LA-UR-23-23023
Accepted Manuscript

Atomic-Scale Modeling of C/N Kinetic Stability Descriptors for PGM-free Electrocatalysts at Finite Temperatures

Holby, Edward F.
Hafiz, Hasnain
Zelenay, Piotr

Provided by the author(s) and the Los Alamos National Laboratory (2023-08-11).

To be published in: Applied Catalysis B: Environmental

DOI to publisher's version: 10.1016/j.apcatb.2023.123158

Permalink to record:
https://permalink.lanl.gov/object/view?what=info:lanl-repo/lareport/LA-UR-23-23023

Atomic-Scale Modeling of C/N Kinetic Stability Descriptors for PGM-free Electrocatalysts at Finite Temperatures

Hasnain Hafiz, Piotr Zelenay, Edward F. Holby

PII: S0926-3373(23)00801-9

DOI: https://doi.org/10.1016/j.apcatb.2023.123158

Reference: APCATB123158

To appear in: *Applied Catalysis B: Environmental*

Received date: 24 March 2023
Revised date: 19 July 2023
Accepted date: 6 August 2023

Please cite this article as: Hasnain Hafiz, Piotr Zelenay and Edward F. Holby, Atomic-Scale Modeling of C/N Kinetic Stability Descriptors for PGM-free Electrocatalysts at Finite Temperatures, *Applied Catalysis B: Environmental,* (2023) doi:https://doi.org/10.1016/j.apcatb.2023.123158

Atomic-Scale Modeling of C/N Kinetic Stability Descriptors for PGM-free Electrocatalysts at Finite Temperatures

Hasnain Hafiz[1], Piotr Zelenay[2], and Edward F. Holby[1,*]

[1] Theoretical Division, Los Alamos National Laboratory, Los Alamos, NM 87545, USA
[2] Materials Physics and Applications Division, Los Alamos National Laboratory, Los Alamos, NM 87545, USA

Abstract

The durability of platinum group metal-free (PGM-free) electrocatalysts is a major barrier to their usage in polymer electrolyte fuel cell cathodes. C and N removal from active sites may play an important role in the catalyst's ability to maintain high activity. While C degradation mechanisms are kinetically controlled, previous studies have focused on thermodynamic descriptors. In this work, we develop a temperature-dependent kinetic descriptor of C and N stability using an electron beam-damage model. Our approach considers the electron beam energy threshold (EBET) describing the knock-on displacement of C and N atoms as a stability descriptor for atomic structures. The stability of different sites is calculated to be different showing this approach can discriminate between similar sites with varied configurations. In addition, we provide important insight regarding TEM beam damage of proposed active sites. We calculate 60 keV electrons can damage some proposed active site structures even at room temperature.

Introduction

The development of highly active, stable, and low-cost platinum group metal-free (PGM-free) electrocatalysts could play an important role in speeding the commercialization of polymer electrolyte fuel cell (PEFC) technology.[1–5] While PGM-free electrocatalysts may ultimately match or even improve upon the catalytic performance of PGM catalysts[6], successful implementation of PGM-free catalysts is presently limited by their insufficient long-term durability under dynamic fuel cell operating conditions. For example, state-of-the-art PGM-free-based PEFCs can only operate for hundreds of hours, whereas their PGM counterparts can go beyond thousands of hours.[7–9] Recent studies show that this substantial loss in activity of PGM-free catalysts originates from the interplay of various degradation mechanisms of active sites, where carbon (C) and nitrogen (N) stability has been proposed to play a vital role, along with demetallation[10,11], active site poisoning[12], and loss of reactant transport pathways with aging.[13]

The active sites in PGM-free electrode materials are often assigned to FeN_4C_x structures that are integrated directly into the host carbon. Therefore, the configurations and stability of C and N impacts the local character and may facilitate the loss of the embedded active sites leading to a reduction in activity for oxygen reduction reaction (ORR). Previous atomistic studies[14–23] that aim to quantify relative stability between active site structures mainly utilize the first-principles derived formation energies which can be useful to assess the likelihood of the formation of a given chemical defect, such as FeN_4, in a host C structure. However, C corrosion to CO or CO_2 in particular is known to be a kinetically controlled process with even graphite being thermodynamically unstable at most fuel cell-relevant potentials.[24,25] A key question that remains unanswered is how the inclusion of kinetic considerations in C/N corrosion, which is absent in these previous, thermodynamic approaches, impacts the relative stability of proposed atomic-scale structures. There is a need to include the kinetics for C and N removal in atomistic models to identify sites with both high activity and high stability against C/N degradation.

A previous atomistic study[26] proposed a quantum chemistry-based descriptor for C/N kinetic stability in PGM-free active sites by invoking an electron beam-damage model[27] from the field of transmission electron microscopy (TEM). The proposed hypothesis was that the knock-on displacement threshold energy (KODTE) in TEM could serve as a durability descriptor for a given atomic structure, enabling quantification of C/N stability without needing details of the exact degradation/corrosion process. The KODTE is defined as the minimum amount of kinetic energy transferred to an atom in a lattice required to liberate it from its bound state. While KODTE has been used in earlier studies for comparing the kinetics of bond breaking of the same atomic species between different structures (in particular, C), it is fundamentally limited when comparing kinetics between different atomic species because of its dependence on atomic mass of the target atom. In TEM experiments, electron kinetic energies are relatively constant with the kinetic energies imparted to given atoms during collision events depending upon their masses. Thus, the more experimentally relevant electron kinetic energy values can instead be used when considering knock-on damage of atoms of varied speciation, leading to the electron beam energy threshold (EBET). We define EBET as the calculated minimum electron beam energy needed to liberate a knock-on atom from its bound state. This is a subtle but important difference when considering both C and N in the same study. An illustrative example is given in the Computational Methods section highlighting this difference. Thus, we will report EBET values as our descriptor for PGM-free ORR active site C/N stability. In summary, EBET and KODTE are mathematically related (see Computational Methods) with the main difference being focusing on the energy of the electron beam for EBET which is experimentally controllable and constant across species of varied masses.

In addition to this usage of EBET, the current study considers an EBET-based stability descriptor at temperatures above 0 K, which was beyond the scope of previous KODTE-based atomistic studies of PGM-free active site models. Prior work utilized a static model of structures which can be useful for delineating relative stability trends, but it cannot answer useful questions regarding the likely durability of structures at given temperatures and given electron beam energies. We show that these temperature effects can play an important role in determining C/N stability under experimental conditions. This inclusion makes possible the direct linking of models and TEM studies to determine local corrosion susceptibility as well as likely conditions for beam damage to occur. One prior study of TEM beam damage did include temperature dependencies[28] and we follow a similar approach here. By integrating ab initio molecular dynamics (AIMD) and density functional tight-binding (DFTB) approaches, we develop an atomistic framework that quantifies the kinetic breaking of the local C/N bonding environment at finite temperatures. This approach provides stability descriptors for C and N at finite temperatures based on an explicit description of the bond-breaking kinetics. It must be emphasized that this approach considers only the removal of C and N atoms from that lattice along with local, finite-temperature-induced, atomic position/velocity fluctuations of the active site structures and is insensitive to any chemical and environmental effects such as pH, electric potential, local liquid/gas phase concentration that may affect degradation reaction rates as well. However, our study demonstrates that despite these assumptions, it is possible to make testable predictions through calculating EBET values of several PGM-free active site structures which can then be tested against TEM experimental observations under varied beam energies and temperatures. Our findings indicate that the thermal perturbations of atoms from their equilibrium positions affect the EBET distributions at finite temperatures for all the active site structures that we considered and variations between sites produce meaningful, comparative values.

Computational Method

In this work, we incorporate the concept of (quasi-)elastic scattering to estimate the electron beam energy that can make knock-on damage to a single atom on a 2D catalyst surface (Fig. 1). During this scattering process, the momentum and energy are transferred from an incoming electron to a target atomic nucleus (C or N) which is typically in motion and displaced from its lattice position due to thermal fluctuations. Depending on the initial electron beam energy, the elastic energy transfer to the atomic nucleus in a backscattering event (scattering angle, $\theta = 180°$) becomes maximum and could be high enough to break the atomic bonds between the target atom and its neighbors, dislodging the target atom out of its lattice. Using relativistic energy-momentum formulations, the maximum energy transfer ($E_{k,v}$) by an electron with beam energy (E_e) to a nucleus with mass M and velocity v parallel to the beam can be expressed as [27],

$$E_{k,v}\left(E_{e,}\theta, v\right) = \frac{2\left(E_e\left(E_e+2mc^2\right)+\sqrt{E_e\left(E_e+2mc^2\right)Mvc}\right)(1-cos\theta)+(Mvc)^2}{2Mc^2} \tag{1}$$

Here m is the electron rest mass, c is the speed of light and θ is the scattering angle. During a backscattering event ($\theta = 180°$), the maximum kinetic energy is transferred to the target atom by the electron beam. The EBET (E_d^v) is defined as the minimum electron beam energy ($E_e = E_d^v$) in a backscattering ($\theta = 180°$) event that displaces the bound target atom from its lattice. This is a function of atomic displacement and velocity, an important consideration when considering thermal effects. The resultant energy transfer during this knock-on event can be written as,

$$E_{k,v}^{max}(E_d^v, \theta = 180°, v) = \frac{(2\sqrt{E_d^v(E_d^v+2mc^2)}+Mvc)^2}{2Mc^2} \tag{2}$$

The maximum energy that an electron with beam energy E_d^0 can transfer to a nucleus at rest ($v = 0$) and creates a knock-on displacement (static, 0 K approximation) becomes,

$$E_{k,0}^{max}(E_d^0, \theta = 180°, v = 0) = \frac{2E_d^0(E_d^0+2mc^2)}{Mc^2} \tag{3}$$

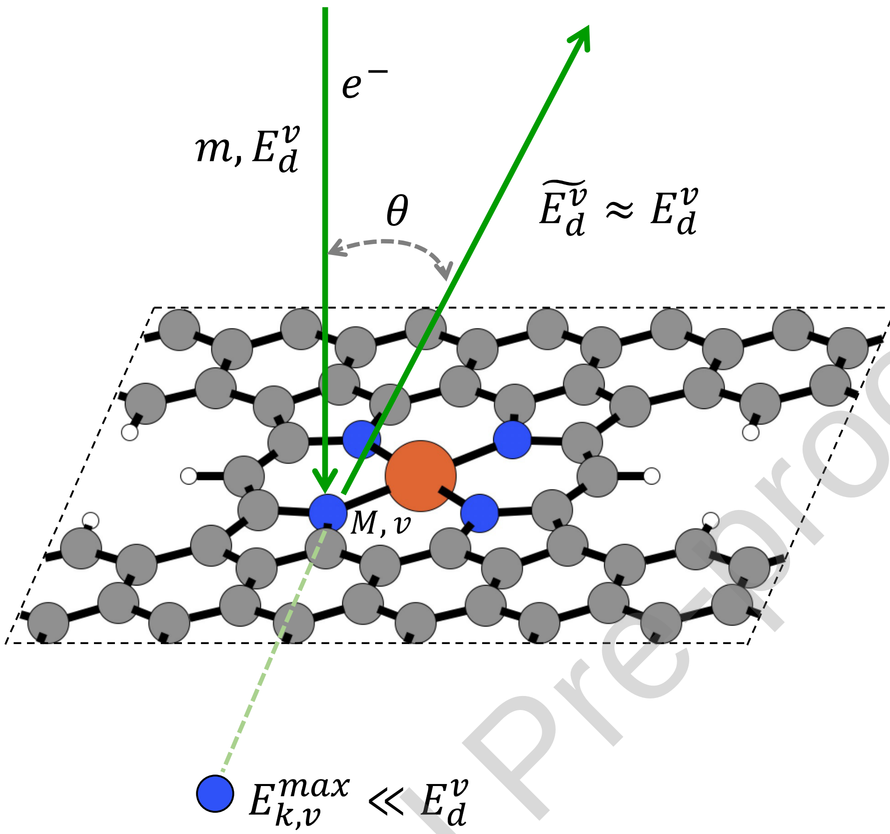

__Figure 1__ A schematic of TEM elastic scattering knock-on damage of N atom on a FeN_4C_x catalyst surface. The kinetic energies of the electron before and after the collision are E_d^v (minimum electron kinetic energy that ejects knock on atom) and $\widetilde{E_d^v}$ respectively.

These equations enable us to show explicitly the difference between EBET and KODTE descriptors. In the static 0 K approximation, the EBET values are equal to the maximum energy transfer E_d^0. To include thermal fluctuations at T > 0 K, we need velocity and displacement corrections of the static EBET values. Using Eqs. 2 and 3, the EBET (E_d^v) for a nucleus moving with velocity v parallel to the beam can be estimated by comparing the maximum energy transfer $\left(E_{k,0}^{max}\right)$ to a nucleus at rest and the maximum energy transfer $\left(E_{k,v}^{max}\right)$ to a nucleus moving with velocity v. Note that the EBET for a moving atom (E_d^v) could be lower or higher than that of a rest atom (E_d^0) depending on the direction of the moving atom's velocity relative to the beam. We assume that $E_d^v < E_d^0$ when v is along the direction of the electron beam and $E_d^v > E_d^0$ when v is in the direction opposite to the electron beam. Based on the above discussion, by approximating $E_{k,v}^{max} \approx E_{k,0}^{max}$, we can rearrange Eq. 2 as follows,

$$E_{k,0}^{max} - v\sqrt{2ME_{k,0}^{max}} + \frac{Mv^2}{2} = \frac{2E_d^v(E_d^v+2mc^2)}{Mc^2} = \text{KODTE}\ (v) \quad (4)$$

The left side of Eq. 4 provides the effective maximum energy transfer for a knock-on process by an electron to an atom moving with velocity v. The middle expresses this effective maximum energy transfer in terms of EBET (E_d). In the case of the static 0 K approximation, Eq. 4 reduces to Eq. 3. This maximum energy transfer for a knock-on process has been defined as the KODTE descriptor[26] which is mathematically related to EBET as described in Eq. 4 in the more general case where atomic velocity is considered.

The dependence on mass, M, in Eq. 4 highlights why KODTE is not a readily transferable descriptor when comparing different atomic species considering a fixed TEM beam energy as suggested before. To highlight this quantitatively and demonstrate our choice of EBET as a kinetic stability descriptor, we consider an N atom and an undercoordinated C atom in a FeN_4C_{12} structure (Fig. 4c). KODTE values at 0 K (static approximation) for the N atom and undercoordinated C atom are 17 eV and 18.1 eV respectively (see Table S2). This would suggest that the N atoms are more susceptible to kinetic bond breaking than the undercoordinated C atoms. However, the corresponding EBET values are calculated to be 99 keV and 91 keV at 0 K (static approximation) respectively which indicates that the undercoordinated C atoms will be damaged at lower electron beam energies than the N atoms, in contrast to the KODTE conclusion. This is due to the deviations in mass between the two species which shifts trends when similar KODTE values are calculated. It is of note, however, this is exactly the case we believe often impacts C/N in our structures of interest. Our example shows that for atoms of different species/mass, EBET is a more consistent descriptor for a given active site with multiple species. Furthermore, EBET enables more direct connection with TEM experiments, being a controlled experimental parameter, which is independent of knock-on species. For a fixed energy impulse leading to a degradation event, we believe that EBET provides a better stability descriptor for C/N for the same reason. Therefore, in this study, we adopt EBET as a kinetically-relevant active site stability descriptor that provides relative susceptibility of bond breaking of an atomic site and is also relevant for TEM beam damage studies, all while being agnostic to atomic species of the knock-on atom.

We next describe how the above methodology can be combined with ab initio molecular dynamics (AIMD) and density functional tight binding (DFTB)-based MD simulations in order to calculate the temperature-dependent EBET of N and C atoms embedded in various proposed FeN_4C_x PGM-free active site structures. Our calculations consider a two-step approach. First, we perform AIMD simulations of the system to calculate the (static, 0 K) EBET as a function of perpendicular atomic displacement of N/C atoms in a given atomic structure. This is needed since thermal fluctuations perturb atoms from their lowest-energy lattice positions which can dramatically impact EBET. Single-layer 6x6 and 6x8 graphene structures are considered to model the basal plane and the edge FeN_4C_x configurations considered, respectively, with a vacuum spacing in the direction perpendicular to the graphene plane of ∼15 Å between periodic slabs. We consider generalized gradient approximation in the form of Perdew-Burke-Ernzerhof's exchange-correlation functional[29,30] as implemented in the Vienna ab initio simulation package (VASP).[31–34] All the initial geometries prior to displacements are optimized self consistently using density functional theory (DFT) with cell shape fixed to that of bulk graphene, allowing ionic but not volume relaxations. Using these optimized FeN_4C_x structures, we carry out a 150 fs AIMD simulation where symmetry equivalent N/C atoms at rest are given some initial kinetic energy. This is implemented in the AIMD as an initial atomic velocity, v_i, commensurate with Eqn. 3 such that

$$E_{k,0}^{max}(E_d^0, \theta = 180°, v = 0) = \frac{2E_d^0(E_d^0+2mc^2)}{Mc^2} = \frac{1}{2}Mv_i^2 \quad (5)$$

Eqn. 5 links the AIMD initial velocity, v_i, to the imparted knock-on energy of an electron beam with energy E_d^0. Therefore, the AIMD-derived EBET values obtained can be considered as the EBET values for the static approximation, where the EBET (E_d^0 in Eqs. 3 and 5) results in kinetic energy transfer ($E_{k,0}^{max}$ in Eqs. 3 and 5) needed for damage when an N/C atom has zero velocity along the beam direction. As the atoms have no net velocities the static approximation of the maximum energy transfer is assumed. By scanning over v_i values in the AIMD calculations, the E_d^0 value that corresponds to EBET value are found for various perpendicular z-displacements of the knock-on atom with respect to lattice plane from their equilibrium 0 K positions. For a given z-displacement, we consider the lowest applied energy (in a range of values separated by 1 keV) that is large enough to eject the N/C atom *ca.* 4 Å from the lattice plane and create an on-site vacancy in the lattice to be the associated 0 K EBET value. A time step of 0.5 ps is chosen which gives an accurate prediction of the dynamics, as previously reported by Su et al.[35]. All calculations consider spin polarization, a plane wave cutoff energy of 560 eV, and a gamma point k-mesh. In addition, the effects of van der Waals interactions are introduced by the dispersion forces using the DFT-D2 method of Grimme,[36] and dipole correction along the z-direction is assumed to avoid spurious interactions between repeated images. The self-consistent electron density loop converged to 10^{-5} eV for AIMD and structural relaxations, and the ionic relaxation loop was run until calculated forces were less than 0.02 eV/Å for structural relaxations.

Second, we obtain temperature-dependent EBET values considering velocity corrections to AIMD-derived EBET values with atomic displacements. The treatment assumes that thermal fluctuations in velocity contribute to the elastic energy transfer as a correction to the total kinetic energy term in Eq. 2, thus leading to a distribution of EBET values based on velocity and out-of-plane-displacement distributions. These velocity and displacement distributions as a function of temperature are added to this model. To account for these thermal effects, DFTB-based MD simulations are performed on the optimized FeN_4C_x structures to obtain displacements and in/out of plane velocity distributions of atoms at temperatures T = 100 K, 300 K, and 500 K. We utilize the DFTB package implemented in Amsterdam Density Functional (ADF) modeling suite[37,38] and consider a self-consistency loop for the Mulliken charges (SCC-DFTB). We use a time step of 0.2 fs and carry out 100 ps MD simulations at different temperatures with the Berendsen thermostat. The Slater-Koster parameters 'trans3d-0-1' for transition metal elements[39] are used as DFTB parameters, and a gamma point is used to sample the Brillouin zone. The MD trajectories are collected with a sampling frequency of 10 (every 2 fs) and normal distributions of probabilities for the displacements and velocities are obtained at a temperature T based on these statistics. These displacement and velocity statistics as a function of temperature are used to determine the probability distribution for the EBET following the AIMD-derived EBET vs. displacement and velocity corrections to Eq. 2. In summary, the velocity and displacement values sampled through MD are applied to the pre-determined EBET values as functions of displacement and velocity to give a distribution of EBET values at a given temperature. This is then fit to a normal distribution such that mean and standard deviation can be easily reported as temperature-dependent stability descriptors. These fits match obtained EBET distributions as shown in Figure 6 and serve as a way of describing the temperature-dependent EBET distribution/stability descriptors using 2 quantitative values.

Results and Discussion

Figs. 2 and 3 show the 0 K EBET values for C and N atoms embedded in bulk graphene and edge structures obtained from AIMD calculations. Considering static nucleus approximations, these energy values correspond to an incident electron beam that transfers the minimum kinetic energy to the targeted nucleus that can create a permanent vacancy in these structures and damage the targeted sites if these C and N atoms are at rest. In reality, these atoms are under thermal motion and as such, a knock-on process may happen under considerably lower electron beam energy values due to atomic displacements and velocities. Thus, these EBET values provide a simplified description of the kinetic durability of these specific sites before thermal contributions are added. Fig. 2a shows that the EBET value for a C atom in pristine graphene is 113 keV which is the highest of all the graphene-based structures we considered. This EBET value corresponds to a 22.92 eV kinetic energy transfer by an electron to a C nucleus which is very close to the earlier reported DFT value of 21.14 eV by Susi et al[40] and high-resolution TEM experimental value of 23.43 eV by Meyer et al[41]. Note that earlier studies[26,40] also reported that the choice of DFT exchange-correlation functional can impact the total kinetic energy transfer and so is an assumption of our model. Despite this assumption, our method obtains a kinetic energy transfer value that is only 0.51 eV lower than the experimental value confirming the accurate description of related kinetics within the static nucleus.

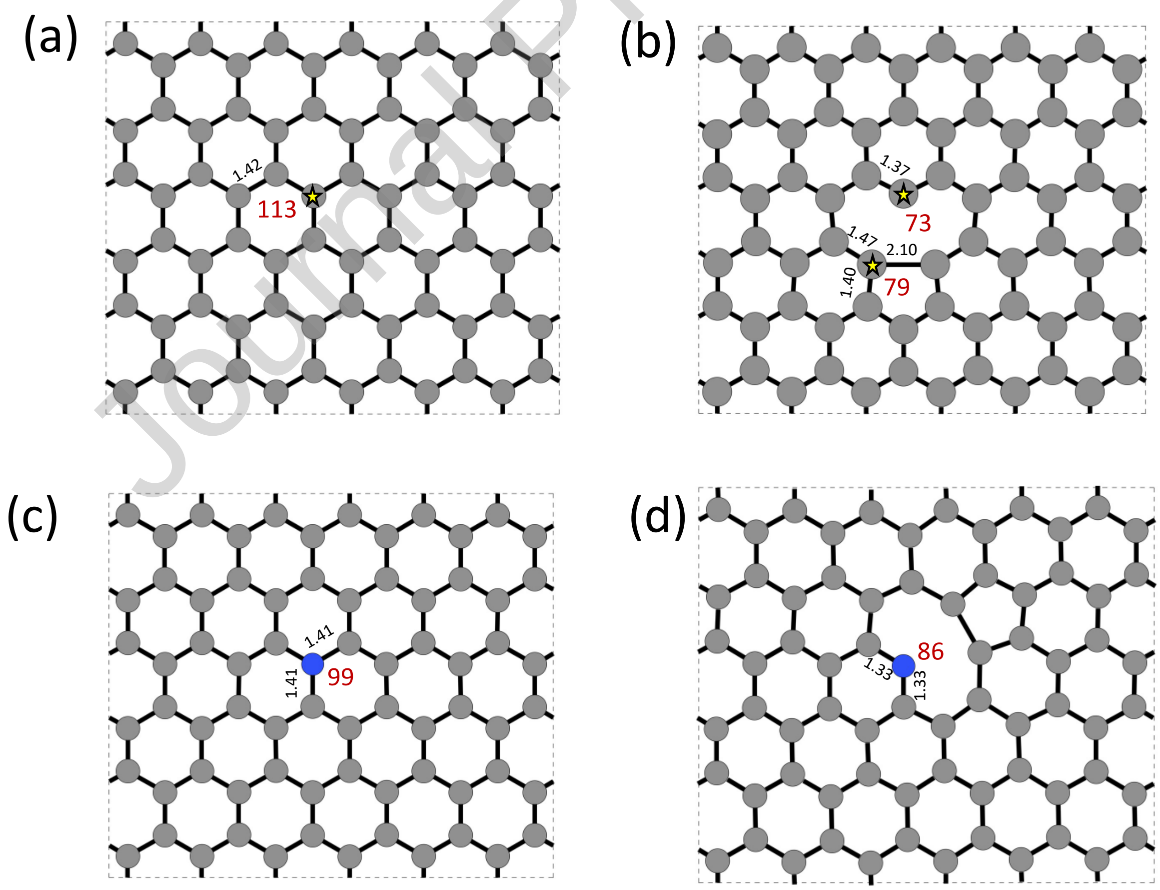

***Figure 2**: Calculated 0 K EBET values for C and N atoms in bulk graphene with and without defects. (a) C atom in pristine graphene, (b) C atom in bulk graphene with a mono vacancy, (c) N atom-doped in bulk graphene, (d) N atom doped in bulk graphene with an adjacent monovacancy. Unit of EBET, reported in red, is in keV. C-C and C-N bond lengths, reported in black, are in Å. C and N atoms are shown in grey and blue colors respectively.*

The presence of a C vacancy can significantly reduce the 0K EBET values. Fig. 2b shows that the C atoms near a monovacancy are more susceptible to beam damage where their EBET values depend on their specific bonding position in the lattice. The C atom in a zigzag site has a lower EBET value of 73 keV whereas the C atom on the armchair site has an EBET value of 79 keV. The corresponding kinetic energy transfer to the targeted atom by the incident electron beam is 14.28 eV and 15.54 eV respectively. These values are close to previously reported DFTB results[42] of 12.96 eV to 14.00 eV and previous DFT result[26] of 15.60 eV. The monovacancy introduces a local C-C strain in the structure which affects the corresponding EBET values of these sites. The C atom next to an armchair edge in a monovacancy is coordinated with three neighboring C atoms resulting in extended C-C bond lengths because of the formation of a five-member ring (see Figure 2b). On the other hand, the C atom next to a zigzag edge in a monovacancy is under-coordinated with two neighboring C atoms resulting in shorter C-C bond distances. As a result, in a monovacancy, the C atom in an armchair edge position has a higher EBET value than the C atom at the zigzag edge position, as shown in Figure 2b. The substitutional doping of a C site with a N atom in pristine graphene reduces the EBET values to 99 keV as shown in Fig. 2c which could be attributed to the local change of electronic structure due to the additional electron in the N 2p shell. Similar to the undoped graphene, a monovacancy defect neighboring the knock-on N atom substitutional also reduces the N atom EBET value to 86 keV as shown in Fig. 2d. We calculate that when an N atom is doped near a monovacancy, the EBET values increase compared to the EBET values of C atoms next to a similar monovacancy (86 keV vs. 73 and 79 keV) indicating a strain effect with shorter bond lengths between neighboring atoms (C-N bond length is 1.33 Å) than that of a monovacancy defected graphene (C-C bond length is 1.37 Å or higher).

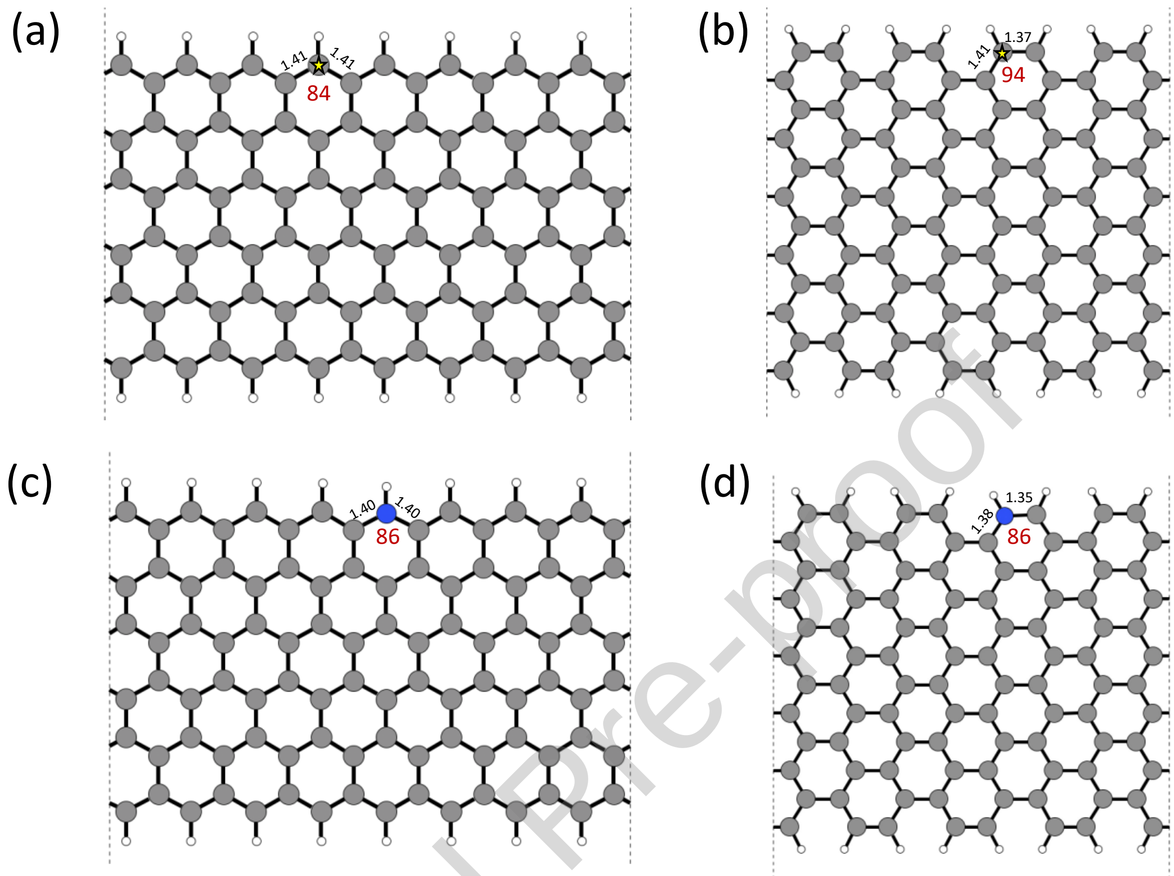

Figure 3: *Calculated 0 K EBET values for C and N atoms in graphene nanoribbon edge structures. (a) C atom at graphene nanoribbon zigzag edge, (b) C atom at graphene nanoribbon armchair edge, (c) N atom at graphene nanoribbon zigzag edge, (d) N atom at graphene nanoribbon armchair edge. The unit of EBET values, reported in red, is in keV. C-C and C-N bond lengths, reported in black, are in Å. C and N atoms are shown in grey and blue colors respectively.*

Fig. 3 shows the effect of edge structures on 0K AIMD-derived EBET values for C and N atoms at the zigzag and armchair edges in the graphene nanoribbon model. The C atom on the armchair edge has higher stability with an EBET value of 94 keV than the C atom at the zigzag edge with an EBET value of 84 keV. This supports the inherent thermodynamic stability of armchair edge C atoms which was also reported elsewhere[43,44] (though this can be dependent upon environment and edge termination). The EBET results support that the C atoms at both edges are more stable than C atoms near a monovacancy defect in the basal plane of graphene. Therefore, the more graphitic nature of active sites could improve site stability. Interestingly, the edge termination has no significant effect on the N atom doped at the nanoribbon edges. For both edges, we find edge-

N EBET values of 86 keV, which is also the same as the N atom doped near a monovacancy defect as shown in Fig. 2d.

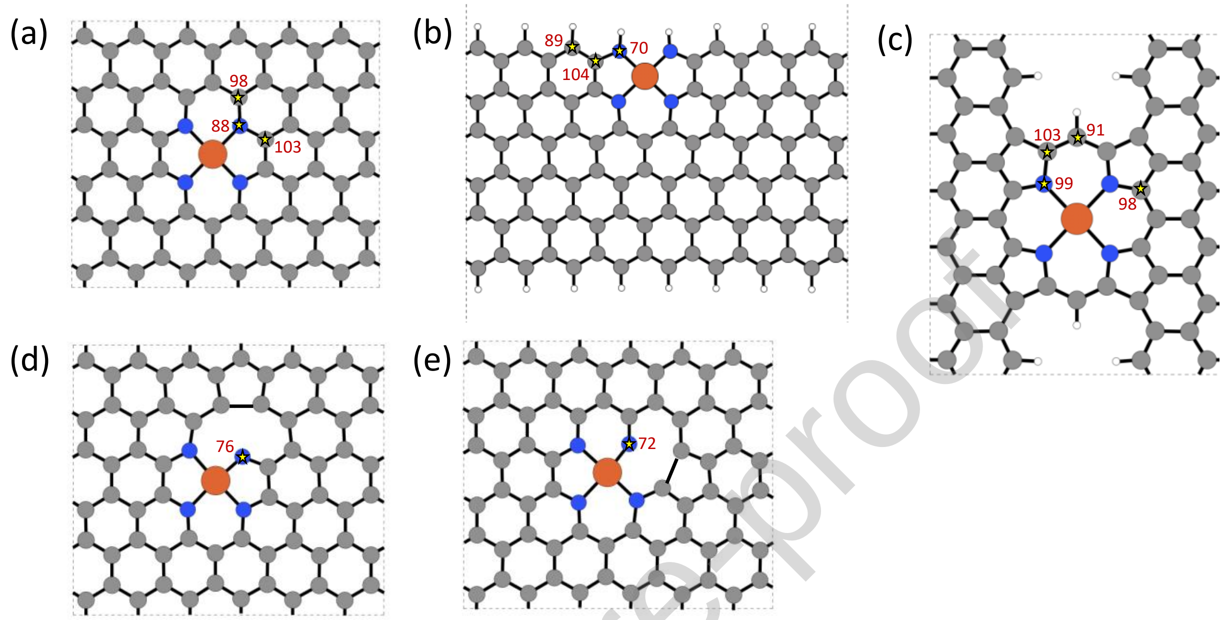

***Figure 4**: Calculated 0 K EBET values for C and N atoms in FeN_4C_x active site structures. (a) FeN_4C_{10} basal plane, (b) FeN_4C_{10} at the zig-zag edge, (c) FeN_4C_{12} basal plane (d) FeN_4C_{10} basal plane structure with C vacancy defects on the zig-zag site, and (e) FeN_4C_{10} basal plane structure with C vacancy defects on the armchair site. The unit of EBET values, reported in red, is in keV. C, N and Fe atoms are shown in grey, blue and orange colors respectively.*

Fig. 4 shows various FeN_4C_x-based PGM-free active site structures and corresponding static approximation EBET values for N and C atoms embedded in these structures. The knock-on displacement threshold energy of Fe was reported to be > 30 eV.[45,46] Such high displacement threshold energy corresponds to an EBET value > 500 keV for Fe, suggesting the metal atom is relatively resistant to (direct) electron beam damage. It is more likely that the adjacent N or C atom could be corroded much before a Fe site is affected by electron bombardment. Therefore, the stability of these N and C supports ultimately affects the kinetic durability of these active site structures. The complex nature of various bonding properties and local strain effects also play a major role on the durability of these active site structures. In the FeN_4C_{10} basal plane structure, the least stable sites are the four N atoms attached to the TM atom with EBET values of 88 keV as shown in Fig. 4a. The nearest neighbors C atoms show significantly larger EBET values of 98 keV and 103 keV which also depend on their specific binding sites. The armchair C atom being a 5-member ring shows higher stability than the zigzag edge C atom in the FeN_4C_{10} basal plane structure. A similar trend for C atoms is also shown in the zigzag edge hosted FeN_4C_{10} structure as shown in Figure 4b. However, the N atoms at the zigzag edge show a significantly lower EBET value of 70 keV, suggesting significantly lower stability of N in the edge hosted FeN_4C_{10} structure. Interestingly, a similar reduction of stability could also be found in defected basal plane structures. The C monovacancy defect near a basal plane FeN_4C_{10} site was calculated to reduce the stability of an undercoordinated N atom with an EBET value of 72 keV as shown in Fig. 4e vs. 88 keV in the undefected structure. The position of the defective site also plays a role in the relative durability of active sites since it can produce different strain effects on the local FeN_4 structure. For example, a monovacancy on the C zigzag site (Fig. 4d) makes the undercoordinated N atom a part of a 5-member ring and can improve the overall stability compared to the case where the monovacancy site is on the armchair edge (Fig. 4e). The most stable structure we have studied so far is the FeN_4C_{12} basal plane structure that shows significantly higher N site stability compared to that of the FeN_4C_{10} basal plane structure. The defected cavity structure in FeN_4C_{12} creates a local stain field that is significantly different from the FeN_4C_{10} structures we considered. Moreover, the symmetric nature of the embedded FeN_4 makes all 4 N atoms part of four 5-member rings and the resultant EBET values are 99 keV as shown in Fig. 4c. The nearest neighbor C atoms of the 5-member ring results in an EBET value of 98 keV and 103 keV which agree well with the EBET values of similar C sites in the FeN_4C_{10} basal plane and zigzag edge hosted structures. However, the undercoordinated C in FeN_4C_{12} shows a lower EBET value of 91 keV compared to its neighboring C atoms. This suggests that the undercoordinated C atom in FeN_4C_{12} dictates the stability of this structure which is still higher than the other FeN_4 structures we considered in which N atoms stability determines the lowest EBET value in the system. Having N as part of a 5-member ring appears to increase calculated EBET values and thus acts to stabilize corresponding active site structures. The effect of defected cavity structure on the stability of FeN_4 active site is also observed in FeN_4C_8 basal plane structure as shown in Fig. S6. While the N atom in FeN_4C_8 shows an EBET value of 96 keV, the undercoordinated C atom (C-C bond length is 2.13 Å, see Fig. S6) results in an EBET value of 75 keV makes the FeN_4C_8 less stable than FeN_4C_{10} and FeN_4C_{12}.

At a finite temperature, the 2D lattice of an active site structure undergoes lattice vibrations. As a result, the atomic position of the target atom experiences displacement fluctuations with respect to its neighboring atoms. Depending on the initial displacement of a target site, the EBET values will be different. Considering the electron beam hits the target atom perpendicular to the lattice plane, we calculate EBET values for C and N atoms for various z-displacements 0 Å – 1.5 Å from the lattice parallel to the beam. Fig. 5 shows the EBET values as a function of z-displacement for various graphene-based and active site structures considered in our study. The highest EBET values shown in any z-displacements are by the C atom in pristine graphene (Fig. 5a). The C atom at the zigzag edge shows considerably lower EBET values for all the z-displacements. The C atom at the zigzag edge with $z = 1.5$ Å results in an EBET value of 18 keV which is 16 keV lower than the C atom in pristine graphene demonstrating the effects of edge termination even if the C atoms are 1.5 Å displaced from the lattice. The N atom in doped graphene shows lower EBET values comparing the C atom in pristine graphene (Fig 4b), however, it results in the highest EBET values for any N atoms in all the FeN_4C_x structures we considered. The N atom in FeN_4C_{12} matches the EBET values of doped graphene at the low displacement but falls to lower values beyond $z = 0.5$ Å. The undercoordinated C atom in FeN_4C_{12} and N atom in the FeN_4C_{10} basal plane show similar EBET results at low displacement, however, at $z = 1.5$ Å displacement the C atom's EBET is 8 keV higher than the N atom. The N atoms in edge hosted and defected FeN_4C_{10} structures show similar EBET as a function of z-displacement. Interestingly, all the N atoms show similar EBET at $z = 1.5$ Å regardless of the local coordination environments where the C atoms for the same displacement show different EBET values for different structures indicating the marked effect of local configurations on EBET.

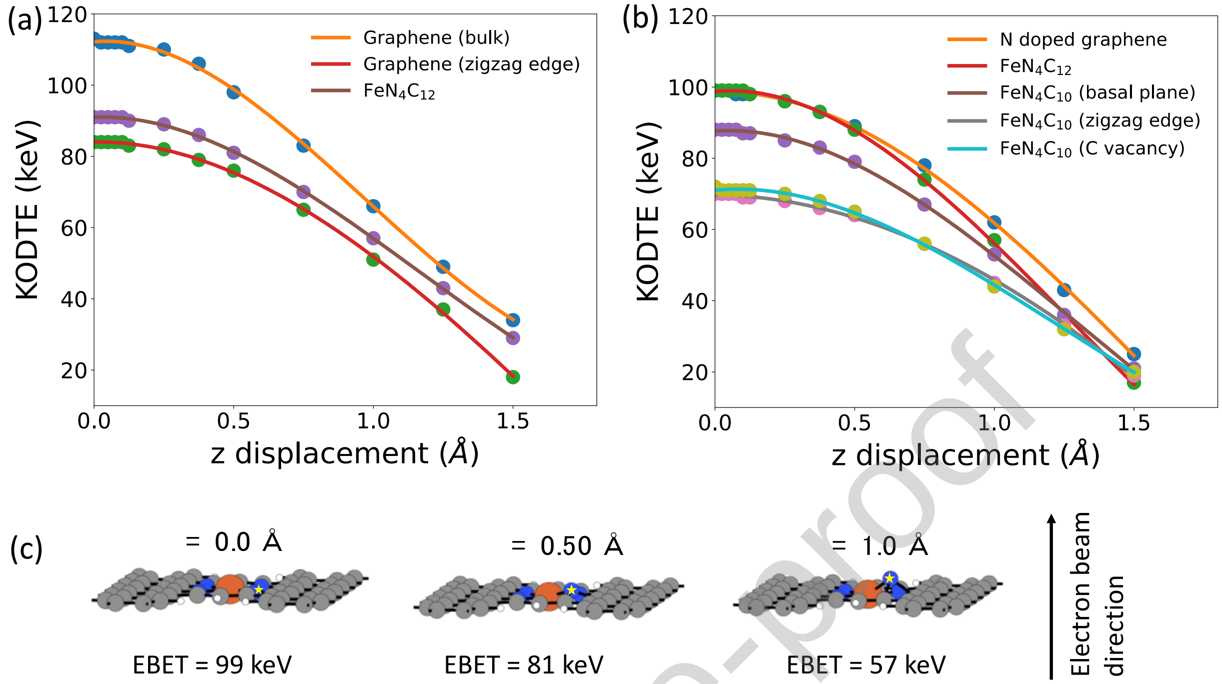

Figure 5*: The EBET of (a) C atom and (b) N atom in considered structures as a function of z-displacement (with no velocity). These serve as input for temperature-dependent EBET distributions. (c) Schematic of initial z-displacement of N atom in FeN_4C_{12} basal plane structure. The displaced N atom is shown with the star mark. C, N, and Fe atoms are shown in grey, blue and orange colors respectively. The coordinated C atom near the defected cavity structure in FeN_4C_{12} is considered in (a). The z-displacement is assumed parallel to the direction of the electron beam.*

To perform temperature correction to the EBET results, we next carry out DFTB MD calculations for T = 100 K, 300 K, and 500 K as described in the Computational Methods section. DFTB trajectories are analyzed and statistical distributions for displacement and velocities are collected. For example, Fig. S1 shows the displacement and velocity distributions of C atoms in pristine graphene at T = 300 K obtained from DFTB MD simulations. At any instant of the MD simulation, the z-displacement of a C or N atom is calculated relative to its nearest neighbor atoms. Therefore, the resultant normal distributions of displacement and velocities show a peak around the equilibrium displacement and velocity which are z = 0 Å and v = $0\,\frac{\text{Å}}{\text{fs}}$ respectively. The AIMD-derived EBET as a function of z-displacement shown in Fig. 5 along with the normal distributions of displacement and velocities are used in Eqs. 2 and 3 to get the temperature-dependent EBET values. Figs. 6a and 6b show the temperature-dependent EBET values for the N atom in FeN_4C_{10} basal plane structure with T = 100 K and 300 K respectively. The distributions get broadened with the temperature indicating that the local fluctuations increase with temperature. Therefore, the mean and standard deviation of these distributions could be useful quantities for the relative comparison of the durability of these structures at finite temperatures. We consider $1\sigma, 3\sigma,$ and 5σ deviations of the EBET values from the mean value (Fig. 6d) which indicates the probability of damage by a TEM electron beam. Considering a typical TEM electron beam with an energy of 60 keV, we find that the N atom in FeN_4C_{10} basal plane is stable at room temperature until the temperature increases to 500 K where it becomes susceptible to corrosion damage, assuming 5σ represents an acceptable tolerance range which is ultimately dependent upon electron flux and dwell time. In contrast, the C atom in pristine graphene (Fig. S2). and the N atom in doped graphene (Fig. S3) show high kinetic stability for all the temperatures we considered in our study to within 5σ.

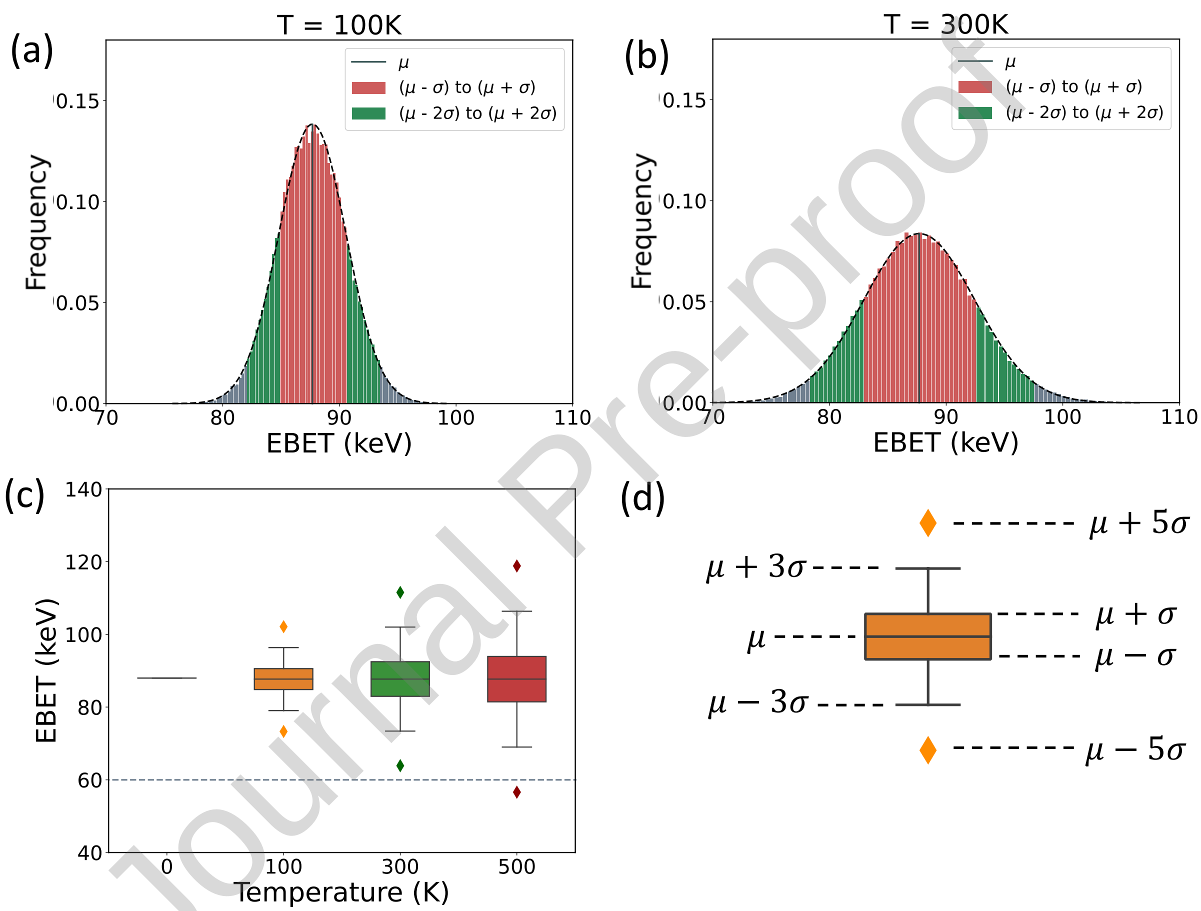

***Figure 6**: The EBET distribution for N atom in FeN_4C_{10} basal plane at (a) T = 100 K and (b) T = 300 K. (c) The mean (μ) and standard deviation (1, 3, 5σ) of temperature-dependent EBET distributions obtained for FeN_4C_{10} basal plane. The horizontal dashed line indicates a typical 60 keV electron beam energy used in TEM experiments (d) The visualization of $1\sigma, 3\sigma$ and 5σ differences from the mean (μ) value of the distribution used in (c) and Fig. 7.*

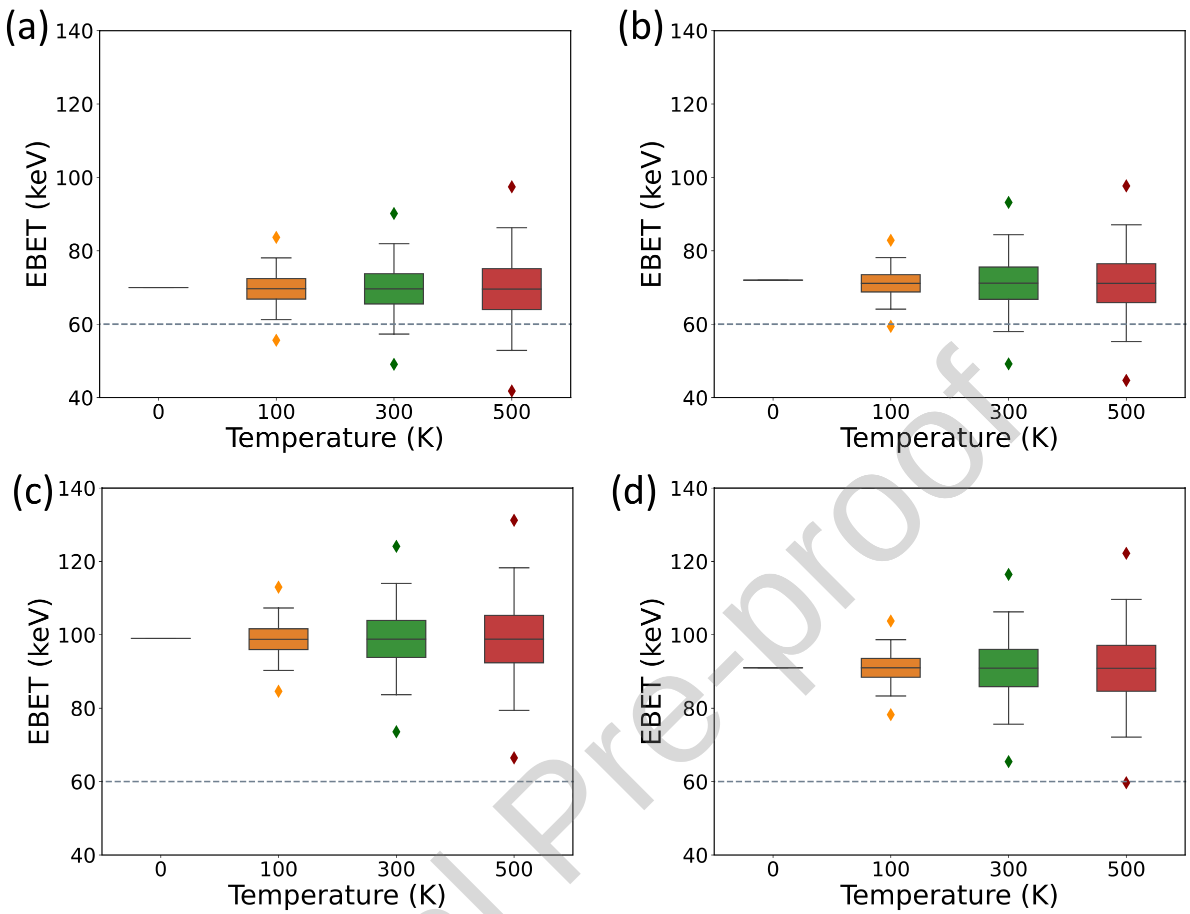

***Figure 7**: The mean (μ) and standard deviations (1, 3, 5σ) of temperature-dependent EBET distributions obtained for (a) N atom in zigzag edge hosted FeN_4C_{10} structure, (b) N atom in defected FeN_4C_{10} basal plane structure, (c) N atom in FeN_4C_{12} basal plane structure, and (d) C atom in FeN_4C_{12} basal plane structure. The horizontal dashed line indicates a typical 60 keV electron beam energy used in TEM experiments. The corresponding EBET distributions at different temperatures are shown in Figs. S4 and S5.*

Considering finite temperature EBET mean and standard deviations between various PGM-free active site structures (see Table S1 in Supplementary Information), we find that edge hosted and vacancy-defected FeN_4C_{10} are highly susceptible to a TEM beam of 60 keV where in both cases the active sites could be damaged by a 60 keV electron beam (see Figs. 7a and 7b) at room temperature. This indicates the poor kinetic stability of these structures in contrast to that of FeN_4C_{10} embedded in the basal plane. The EBET for an N atom in zigzag edge hosted and vacancy-defected FeN_4C_{10} structures can be as low as 57.29 keV and 58 keV respectively within $\mu - 3\sigma$ deviations at T=300 K (see normal distributions in Figs. S4b and S4e) suggesting the N atoms in such sites are less stable compared to others considered. The N atom in FeN_4C_{12} shows superior performance for all the temperatures as shown in Figs. 7c and S5, however, the undercoordinated C in this structure most likely affects its stability at T = 500 K as shown in Fig. 7d and so may be susceptible to damage at elevated temperatures. Note that the N atom in FeN_4C_{10} (Fig. 6c) and C atom in FeN_4C_{12} basal plane structures (Fig. 7d) show similar EBET values at finite temperatures. This indicates that both of these basal plane structures are equally stable at room temperature conditions and unlikely to degrade under electron beam until temperatures increases to 500 K where FeN_4C_{12} is slightly more stable than FeN_4C_{10} (Figs. 7d and 6c and Table S1). Combined, these findings highlight that EBET and, ostensibly, C/N stability are temperature dependent. As the EBET distribution widens with increased temperature, so does the probability of knock-on damage due to thermal fluctuations. While, in general, graphene is a good thermal conductor, local TEM beam heating may still play some role in damage, along with the demonstrated structural dependencies.

Conclusions

By combining AIMD and DFTB simulations we have developed an atomistic framework for calculating stability descriptors for C/N corrosion at finite temperatures and applied it to a variety of possible PGM-free active site structures. We incorporated the concept of the electron beam-damage model and defined the stability descriptor, EBET, in terms of electron beam energies used in TEM experiments. The obtained EBET values provide a relative description of the kinetic stability of various PGM-free active site structures against C/N degradation that we considered in this study. Our study indicates that the C atom in pristine graphene has the highest stability, however, the formation of local vacancies can significantly reduce the overall kinetic stability. We find a trend in the relative kinetic stability of C atoms in carbon structures: pristine graphene > armchair edge > zigzag edge > monovacancy-neighboring structures. The doping of C with N in pristine graphene reduces the overall kinetic stability. Interestingly, when the N atom is positioned near a vacancy or an edge, our results show similar EBET for all the configurations, suggesting a strong dependence of calculated values on the nearest-neighbor coordination environment.

For FeN_4C_x-based PGM-free active site model structures, the complex nature of C and N bonding properties and local strain effects play a major role on the durability of these active site structures. Our results indicate a kinetic stability trend for N removal in considered sites of: FeN_4C_{12} basal plane > FeN_4C_{10} basal plane > FeN_4C_{10} basal plane with C vacancy at zigzag site > FeN_4C_{10} basal plane with C vacancy at armchair site > FeN_4C_{10} at the zig-zag edge. Our study further indicates that when a C or N atom is in a 5-member ring, it shows overall enhanced kinetic stability. The temperature-dependent EBET results reveal a similar stability trend for all FeN_4C_x active site structures where we find that the EBET distributions are affected by the thermal perturbations of atoms from their equilibrium positions. We find that under a 60 keV TEM electron beam the N atom in FeN_4C_{10} basal plane is stable around 300 K, becoming more susceptible to damage at 500 K. The overall stability is reduced for edge hosted and vacancy-defected FeN_4C_{10} structures where the 60 keV TEM electron beam can damage an active site even at 300 K. Finally, the N atom in FeN_4C_{12} shows superior stability even at 500 K and the undercoordinated C in this structure is calculated to limit its overall stability, in contrast to other C/N systems. These findings should be taken into consideration along with proposed metal dissolution-based descriptors. We hypothesize that it is possible for different degradation mechanisms (e.g., C/N corrosion vs. Fe-metal dissolution) to be dominant for different structures and under varied conditions, something that will be the focus of future work within our group. Such knowledge will help not only in understanding how ORR activity is lost in these systems but will also help guide the synthesis of more robust structures in the future.

Supporting Information

Supporting information contains temperature-dependent displacement, velocity, and EBET distributions on different structures that were used for various analyses of this manuscript.

Acknowledgments

Financial support for this work was provided by the US DOE Office of Energy Efficiency and Renewable Energy, Hydrogen and Fuel Cell Technologies Office, under the ElectroCat Consortium, DOE technology managers McKenzie Hubert and William Gibbons, and DOE program managers David Peterson and Dimitrios Papageorgopolous. This research used resources provided by the Los Alamos National Laboratory Institutional Computing Program, which is supported by the U.S. Department of Energy National Nuclear Security Administration under Contract No. 89233218CNA000001.The authors would like to thank Michael Zachman and David Cullen of ORNL for valuable conversations regarding TEM and in situ beam damage.

References

(1) Jaouen, F.; Proietti, E.; Lefèvre, M.; Chenitz, R.; Dodelet, J.-P.; Wu, G.; Chung, H. T.; Johnston, C. M.; Zelenay, P. Recent Advances in Non-Precious Metal Catalysis for Oxygen-Reduction Reaction in Polymer Electrolyte Fuel Cells. *Energy Environ. Sci.* **2011**, *4* (1), 114–130. https://doi.org/10.1039/C0EE00011F.

(2) Jiao, Y.; Zheng, Y.; Jaroniec, M.; Qiao, S. Z. Design of Electrocatalysts for Oxygen- and Hydrogen-Involving Energy Conversion Reactions. *Chem. Soc. Rev.* **2015**, *44* (8), 2060–2086. https://doi.org/10.1039/C4CS00470A.

(3) Wang, W.; Jia, Q.; Mukerjee, S.; Chen, S. Recent Insights into the Oxygen-Reduction Electrocatalysis of Fe/N/C Materials. *ACS Catal.* **2019**, *9* (11), 10126–10141. https://doi.org/10.1021/acscatal.9b02583.

(4) Martinez, U.; Komini Babu, S.; Holby, E. F.; Chung, H. T.; Yin, X.; Zelenay, P. Progress in the Development of Fe-Based PGM-Free Electrocatalysts for the Oxygen Reduction Reaction. *Adv. Mater.* **2019**, *31* (31), 1806545. https://doi.org/10.1002/adma.201806545.

(5) Martinez, U.; Komini Babu, S.; Holby, E. F.; Zelenay, P. Durability Challenges and Perspective in the Development of PGM-Free Electrocatalysts for the Oxygen Reduction Reaction. *Curr. Opin. Electrochem.* **2018**, *9*, 224–232. https://doi.org/10.1016/j.coelec.2018.04.010.

(6) Thompson, S. T.; Wilson, A. R.; Zelenay, P.; Myers, D. J.; More, K. L.; Neyerlin, K. C.; Papageorgopoulos, D. ElectroCat: DOE's Approach to PGM-Free Catalyst and Electrode R&D. *Solid State Ion.* **2018**, *319*, 68–76. https://doi.org/10.1016/j.ssi.2018.01.030.

(7) Serov, A.; Workman, M. J.; Artyushkova, K.; Atanassov, P.; McCool, G.; McKinney, S.; Romero, H.; Halevi, B.; Stephenson, T. Highly Stable Precious Metal-Free Cathode Catalyst for Fuel Cell Application. *J. Power Sources* **2016**, *327*, 557–564. https://doi.org/10.1016/j.jpowsour.2016.07.087.

(8) Shao, M.; Chang, Q.; Dodelet, J.-P.; Chenitz, R. Recent Advances in Electrocatalysts for Oxygen Reduction Reaction. *Chem. Rev.* **2016**, *116* (6), 3594–3657. https://doi.org/10.1021/acs.chemrev.5b00462.

(9) Wu, G.; More, K. L.; Johnston, C. M.; Zelenay, P. High-Performance Electrocatalysts for Oxygen Reduction Derived from Polyaniline, Iron, and Cobalt. *Science* **2011**, *332* (6028), 443–447. https://doi.org/10.1126/science.1200832.

(10) Holby, E. F.; Wang, G.; Zelenay, P. Acid Stability and Demetalation of PGM-Free ORR Electrocatalyst Structures from Density Functional Theory: A Model for "Single-Atom Catalyst" Dissolution. *ACS Catal.* **2020**, *10* (24), 14527–14539. https://doi.org/10.1021/acscatal.0c02856.

(11) Patniboon, T.; Hansen, H. A. Acid-Stable and Active M–N–C Catalysts for the Oxygen Reduction Reaction: The Role of Local Structure. *ACS Catal.* **2021**, *11* (21), 13102–13118. https://doi.org/10.1021/acscatal.1c02941.
(12) Svane, K. L.; Reda, M.; Vegge, T.; Hansen, H. A. Improving the Activity of M−N4 Catalysts for the Oxygen Reduction Reaction by Electrolyte Adsorption. *ChemSusChem* **2019**, *12* (23), 5133–5141. https://doi.org/10.1002/cssc.201902443.
(13) Dubau, L.; Castanheira, L.; Maillard, F.; Chatenet, M.; Lottin, O.; Maranzana, G.; Dillet, J.; Lamibrac, A.; Perrin, J.-C.; Moukheiber, E.; ElKaddouri, A.; De Moor, G.; Bas, C.; Flandin, L.; Caqué, N. A Review of PEM Fuel Cell Durability: Materials Degradation, Local Heterogeneities of Aging and Possible Mitigation Strategies. *WIREs Energy Environ.* **2014**, *3* (6), 540–560. https://doi.org/10.1002/wene.113.
(14) Calle-Vallejo, F.; Martínez, J. I.; Rossmeisl, J. Density Functional Studies of Functionalized Graphitic Materials with Late Transition Metals for Oxygen Reduction Reactions. *Phys. Chem. Chem. Phys.* **2011**, *13* (34), 15639–15643. https://doi.org/10.1039/C1CP21228A.
(15) Holby, E. F.; Taylor, C. D. Control of Graphene Nanoribbon Vacancies by Fe and N Dopants: Implications for Catalysis. *Appl. Phys. Lett.* **2012**, *101* (6), 064102. https://doi.org/10.1063/1.4742890.
(16) Holby, E. F.; Wu, G.; Zelenay, P.; Taylor, C. D. Metropolis Monte Carlo Search for Non-Precious Metal Catalyst Active Site Candidates. *ECS Trans.* **2013**, *50* (2), 1839. https://doi.org/10.1149/05002.1839ecst.
(17) Holby, E. F.; Wu, G.; Zelenay, P.; Taylor, C. D. Structure of Fe–Nx–C Defects in Oxygen Reduction Reaction Catalysts from First-Principles Modeling. *J. Phys. Chem. C* **2014**, *118* (26), 14388–14393. https://doi.org/10.1021/jp503266h.
(18) Holby, E. F.; Taylor, C. D. Activity of N-Coordinated Multi-Metal-Atom Active Site Structures for Pt-Free Oxygen Reduction Reaction Catalysis: Role of *OH Ligands. *Sci. Rep.* **2015**, *5* (1), 9286. https://doi.org/10.1038/srep09286.
(19) Kattel, S.; Atanassov, P.; Kiefer, B. Stability, Electronic and Magnetic Properties of In-Plane Defects in Graphene: A First-Principles Study. *J. Phys. Chem. C* **2012**, *116* (14), 8161–8166. https://doi.org/10.1021/jp2121609.
(20) Kwak, D.; Khetan, A.; Noh, S.; Pitsch, H.; Han, B. First Principles Study of Morphology, Doping Level, and Water Solvation Effects on the Catalytic Mechanism of Nitrogen-Doped Graphene in the Oxygen Reduction Reaction. *ChemCatChem* **2014**, *6* (9), 2662–2670. https://doi.org/10.1002/cctc.201402248.
(21) Chai, G.-L.; Hou, Z.; Shu, D.-J.; Ikeda, T.; Terakura, K. Active Sites and Mechanisms for Oxygen Reduction Reaction on Nitrogen-Doped Carbon Alloy Catalysts: Stone–Wales Defect and Curvature Effect. *J. Am. Chem. Soc.* **2014**, *136* (39), 13629–13640. https://doi.org/10.1021/ja502646c.
(22) Kattel, S.; Atanassov, P.; Kiefer, B. Catalytic Activity of Co–Nx/C Electrocatalysts for Oxygen Reduction Reaction: A Density Functional Theory Study. *Phys. Chem. Chem. Phys.* **2013**, *15* (1), 148–153. https://doi.org/10.1039/C2CP42609A.
(23) Kattel, S.; Atanassov, P.; Kiefer, B. A Density Functional Theory Study of Oxygen Reduction Reaction on Non-PGM Fe–Nx–C Electrocatalysts. *Phys. Chem. Chem. Phys.* **2014**, *16* (27), 13800–13806. https://doi.org/10.1039/C4CP01634C.
(24) Gruver, G. A. The Corrosion of Carbon Black in Phosphoric Acid. *J. Electrochem. Soc.* **1978**, *125* (10), 1719. https://doi.org/10.1149/1.2131280.
(25) *Kinoshita, K., 1988. Carbon: Electrochemical and Physicochemical Properties.*
(26) Holby, E. F. First-Principles Molecular Dynamics Study of Carbon Corrosion in PEFC Catalyst Materials. *Fuel Cells* **2016**, *16* (6), 669–674. https://doi.org/10.1002/fuce.201600012.
(27) Susi, T.; Meyer, J. C.; Kotakoski, J. Quantifying Transmission Electron Microscopy Irradiation Effects Using Two-Dimensional Materials. *Nat. Rev. Phys.* **2019**, *1* (6), 397–405. https://doi.org/10.1038/s42254-019-0058-y.
(28) Chirita Mihaila, A. I.; Susi, T.; Kotakoski, J. Influence of Temperature on the Displacement Threshold Energy in Graphene. *Sci. Rep.* **2019**, *9* (1), 12981. https://doi.org/10.1038/s41598-019-49565-4.
(29) Perdew, J. P.; Burke, K.; Ernzerhof, M. Generalized Gradient Approximation Made Simple. *Phys. Rev. Lett.* **1996**, *77* (18), 3865–3868. https://doi.org/10.1103/PhysRevLett.77.3865.
(30) Perdew, J. P.; Burke, K.; Ernzerhof, M. Generalized Gradient Approximation Made Simple [Phys. Rev. Lett. 77, 3865 (1996)]. *Phys. Rev. Lett.* **1997**, *78* (7), 1396–1396. https://doi.org/10.1103/PhysRevLett.78.1396.
(31) Kresse, G.; Hafner, J. Ab Initio Molecular Dynamics for Liquid Metals. *Phys. Rev. B* **1993**, *47* (1), 558–561. https://doi.org/10.1103/PhysRevB.47.558.
(32) Kresse, G.; Furthmüller, J.; Hafner, J. Theory of the Crystal Structures of Selenium and Tellurium: The Effect of Generalized-Gradient Corrections to the Local-Density Approximation. *Phys. Rev. B* **1994**, *50* (18), 13181–13185. https://doi.org/10.1103/PhysRevB.50.13181.
(33) Kresse, G.; Furthmüller, J. Efficiency of Ab-Initio Total Energy Calculations for Metals and Semiconductors Using a Plane-Wave Basis Set. *Comput. Mater. Sci.* **1996**, *6* (1), 15–50. https://doi.org/10.1016/0927-0256(96)00008-0.
(34) Kresse, G.; Furthmüller, J. Efficient Iterative Schemes for Ab Initio Total-Energy Calculations Using a Plane-Wave Basis Set. *Phys. Rev. B* **1996**, *54* (16), 11169–11186. https://doi.org/10.1103/PhysRevB.54.11169.
(35) Su, C.; Tripathi, M.; Yan, Q.-B.; Wang, Z.; Zhang, Z.; Hofer, C.; Wang, H.; Basile, L.; Su, G.; Dong, M.; Meyer, J. C.; Kotakoski, J.; Kong, J.; Idrobo, J.-C.; Susi, T.; Li, J. Engineering Single-Atom Dynamics with Electron Irradiation. *Sci. Adv. 5* (5), eaav2252. https://doi.org/10.1126/sciadv.aav2252.
(36) Grimme, S. Semiempirical GGA-Type Density Functional Constructed with a Long-Range Dispersion Correction. *J. Comput. Chem.* **2006**, *27* (15), 1787–1799. https://doi.org/10.1002/jcc.20495.

(37) te Velde, G.; Bickelhaupt, F. M.; Baerends, E. J.; Fonseca Guerra, C.; van Gisbergen, S. J. A.; Snijders, J. G.; Ziegler, T. Chemistry with ADF. *J. Comput. Chem.* **2001**, *22* (9), 931–967. https://doi.org/10.1002/jcc.1056.
(38) ADF 2021.1, SCM, Theoretical Chemistry, Vrije Universiteit, Amsterdam, The Netherlands, Http://Www.Scm.Com.
(39) Zheng, G.; Witek, H. A.; Bobadova-Parvanova, P.; Irle, S.; Musaev, D. G.; Prabhakar, R.; Morokuma, K.; Lundberg, M.; Elstner, M.; Köhler, C.; Frauenheim, T. Parameter Calibration of Transition-Metal Elements for the Spin-Polarized Self-Consistent-Charge Density-Functional Tight-Binding (DFTB) Method: Sc, Ti, Fe, Co, and Ni. *J. Chem. Theory Comput.* **2007**, *3* (4), 1349–1367. https://doi.org/10.1021/ct600312f.
(40) Susi, T.; Hofer, C.; Argentero, G.; Leuthner, G. T.; Pennycook, T. J.; Mangler, C.; Meyer, J. C.; Kotakoski, J. Isotope Analysis in the Transmission Electron Microscope. *Nat. Commun.* **2016**, *7* (1), 13040. https://doi.org/10.1038/ncomms13040.
(41) Meyer, J. C.; Eder, F.; Kurasch, S.; Skakalova, V.; Kotakoski, J.; Park, H. J.; Roth, S.; Chuvilin, A.; Eyhusen, S.; Benner, G.; Krasheninnikov, A. V.; Kaiser, U. Accurate Measurement of Electron Beam Induced Displacement Cross Sections for Single-Layer Graphene. *Phys. Rev. Lett.* **2012**, *108* (19), 196102. https://doi.org/10.1103/PhysRevLett.108.196102.
(42) Krasheninnikov, A. V.; Banhart, F.; Li, J. X.; Foster, A. S.; Nieminen, R. M. Stability of Carbon Nanotubes under Electron Irradiation: Role of Tube Diameter and Chirality. *Phys. Rev. B* **2005**, *72* (12), 125428. https://doi.org/10.1103/PhysRevB.72.125428.
(43) Wassmann, T.; Seitsonen, A. P.; Saitta, A. M.; Lazzeri, M.; Mauri, F. Structure, Stability, Edge States, and Aromaticity of Graphene Ribbons. *Phys. Rev. Lett.* **2008**, *101* (9), 096402. https://doi.org/10.1103/PhysRevLett.101.096402.
(44) Seitsonen, A. P.; Saitta, A. M.; Wassmann, T.; Lazzeri, M.; Mauri, F. Structure and Stability of Graphene Nanoribbons in Oxygen, Carbon Dioxide, Water, and Ammonia. *Phys. Rev. B* **2010**, *82* (11), 115425. https://doi.org/10.1103/PhysRevB.82.115425.
(45) Maury, F.; Biget, M.; Vajda, P.; Lucasson, A.; Lucasson, P. Anisotropy of Defect Creation in Electron-Irradiated Iron Crystals. *Phys. Rev. B* **1976**, *14* (12), 5303–5313. https://doi.org/10.1103/PhysRevB.14.5303.
(46) Olsson, P.; Becquart, C. S.; Domain, C. Ab Initio Threshold Displacement Energies in Iron. *Mater. Res. Lett.* **2016**, *4* (4), 219–225. https://doi.org/10.1080/21663831.2016.1181680.

HH and EFH were responsible for research conceptualization and methodology development. Calculations and data analysis were performed by HH along with writing of original draft. EFH and PZ reviewed and edited along with funding acquisition and project administration.

Declaration of interests

☐ The authors declare that they have no known competing financial interests or personal relationships that could have appeared to influence the work reported in this paper.

☒ The authors declare the following financial interests/personal relationships which may be considered as potential competing interests:

Edward Holby, Piotr Zelenay, Hasnain Hafiz reports financial support was provided by Office of Energy Efficiency and Renewable Energy.

Highlights

- Developed and applied descriptor model of electrocatalyst kinetic stability
- Temperature dependence of beam damage model elucidated
- Novel descriptor approach will aid in making better M-N-C electrocatalysts

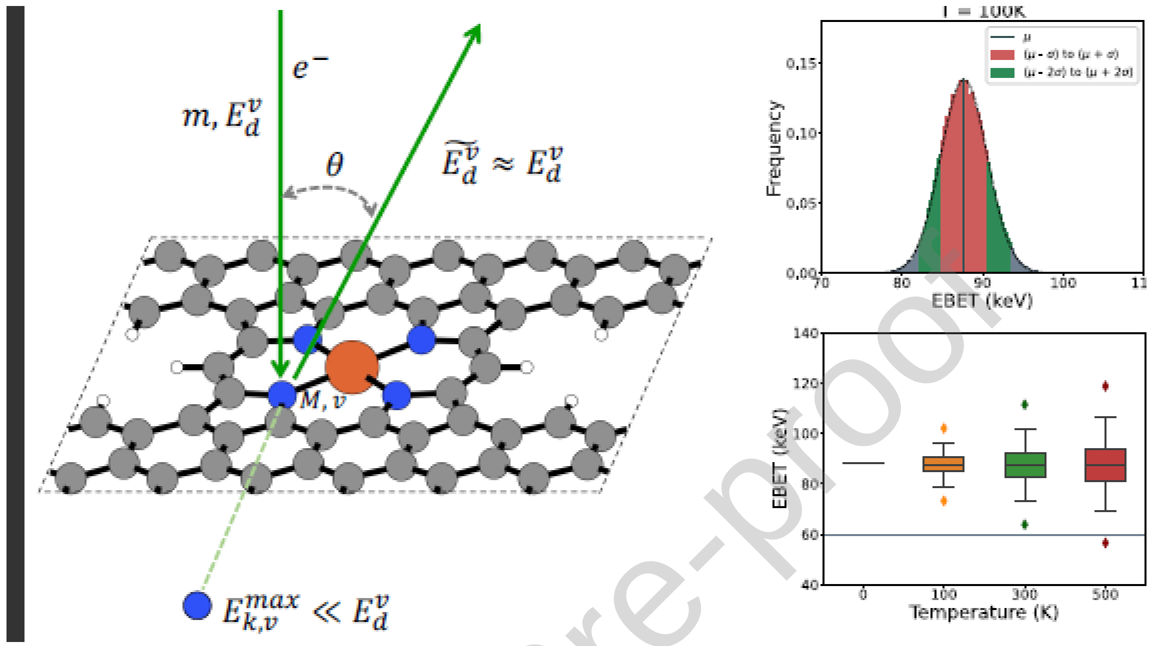

Supporting Information:

Atomistic Modeling of C/N Kinetic Stability Descriptors for PGM-free Electrocatalysts at Finite Temperature

Hasnain Hafiz[1], Piotr Zelenay[2] and Edward F. Holby[3]

[1] Theoretical Division, Los Alamos National Laboratory, Los Alamos, NM 87545, USA
[2] Materials Physics and Applications Division, Los Alamos National Laboratory, Los Alamos, NM 87545, USA
[3] Sigma Division, Los Alamos National Laboratory, Los Alamos, NM 87545, USA

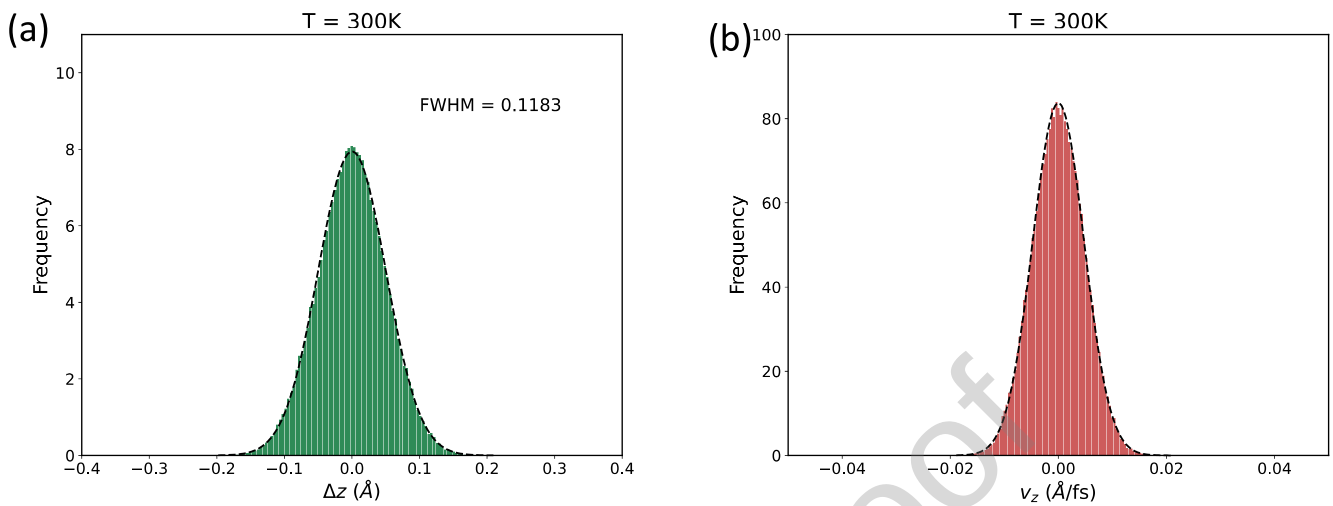

Figure S1*: (a) Displacement and (b) velocity distributions of C atoms in pristine graphene at T= 300 K obtained from DFTB MD simulations.*

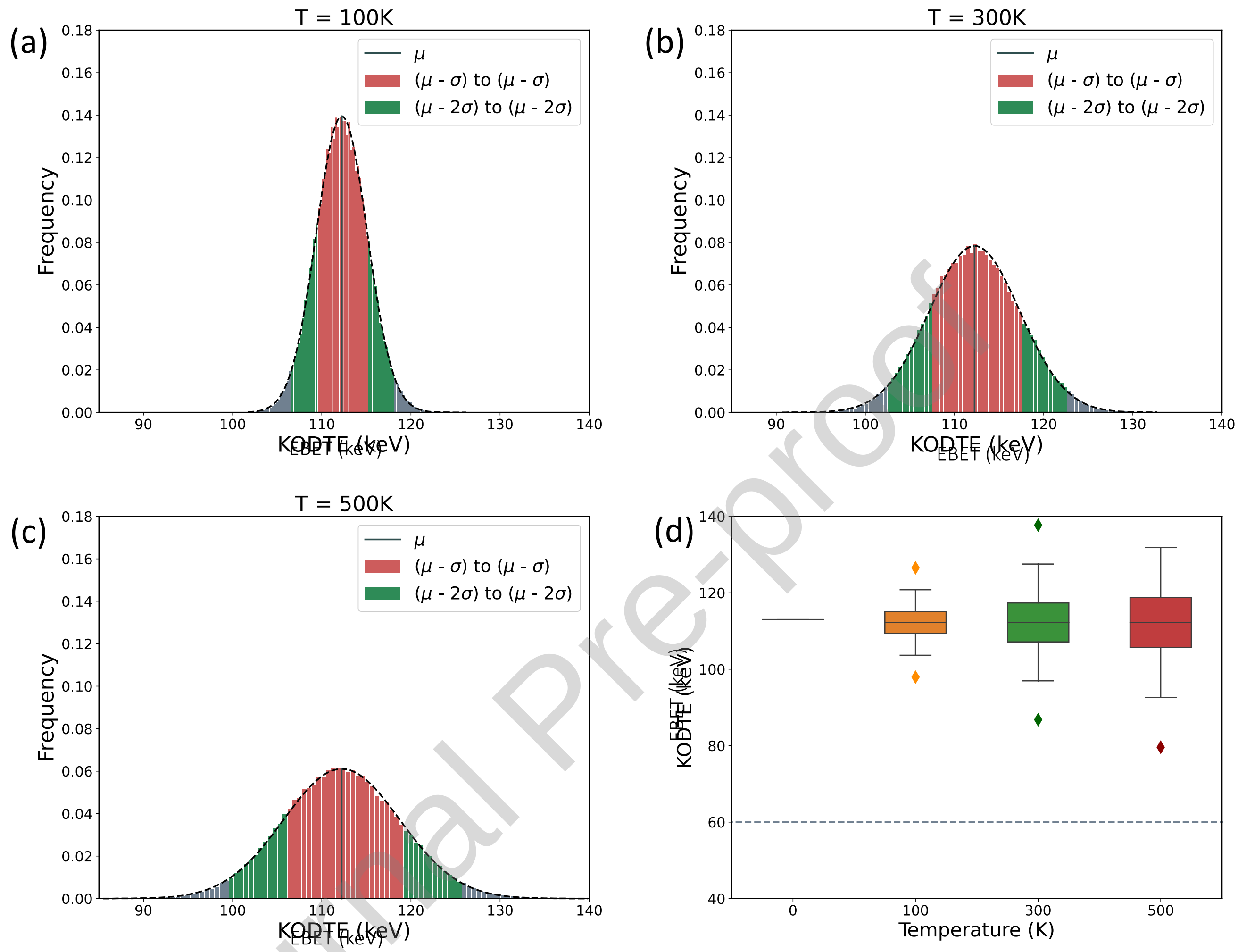

***Figure S2**: The EBET distribution for C atom in pristine graphene at (a) T = 100 K, (b) T = 300 K, and (c) T = 500 K. (d) The mean (μ) and standard deviation (σ) of EBET distributions as a function of temperature. The horizontal dashed line indicates a typical electron beam energy used in the TEM experiment.*

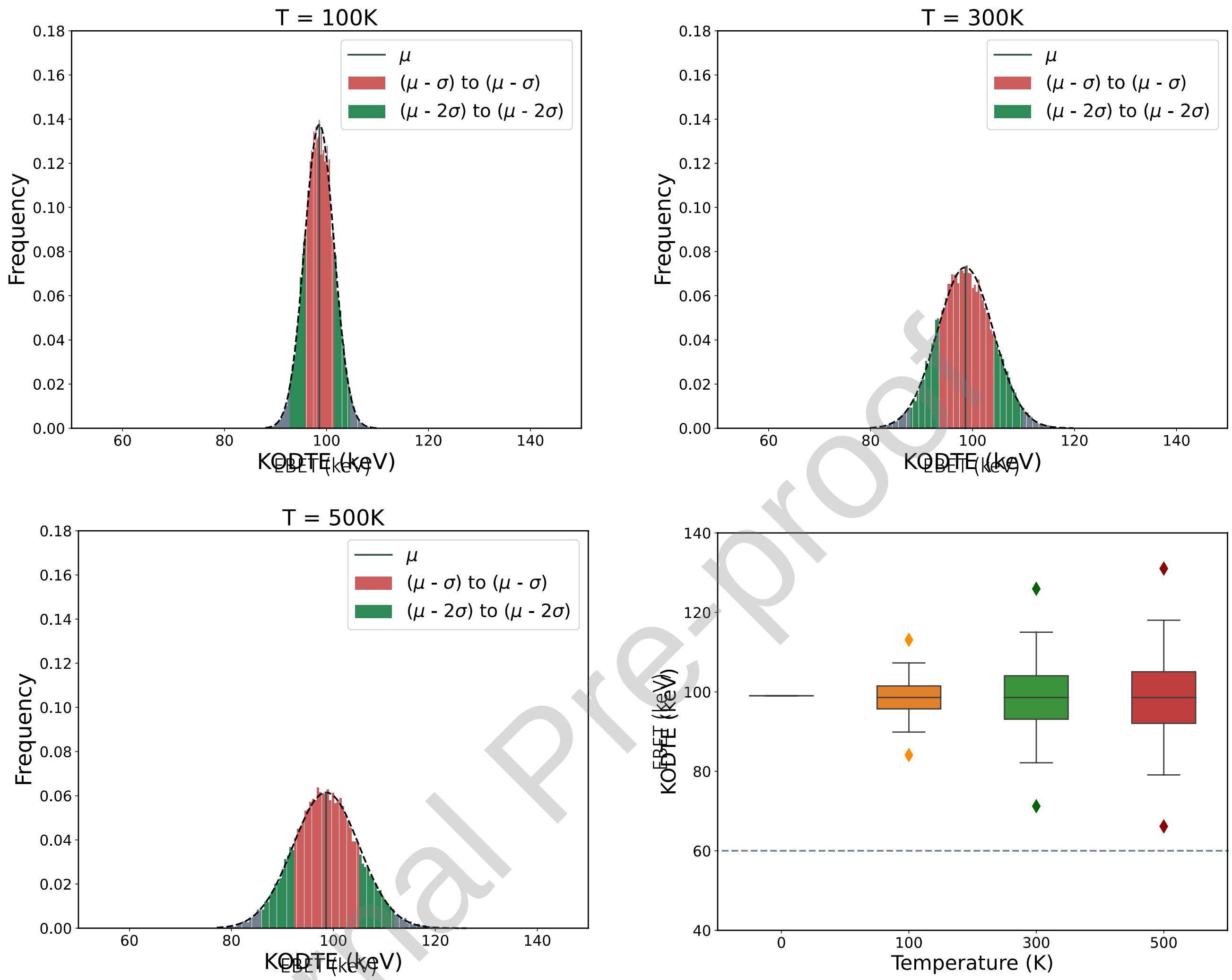

***Figure S3**: The EBET distribution for an N atom which is doped in bulk graphene (structure shown in Fig 2 (c)) at (a) T = 100 K, (b) T = 300 K, and (c) T = 500 K. (d) The mean (μ) and standard deviation (σ) of EBET distributions as a function of temperature. The horizontal dashed line indicates a typical electron beam energy used in the TEM experiment.*

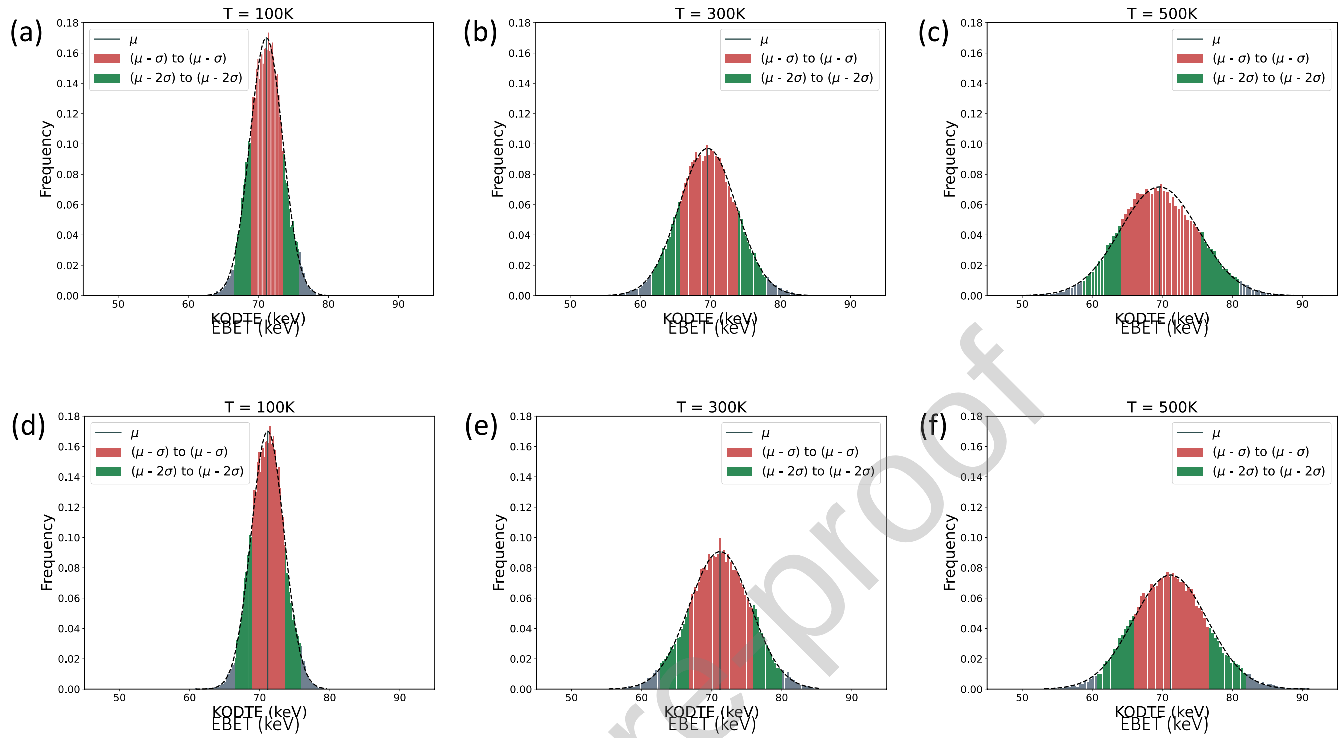

Figure S4*: The EBET distribution for N atom in zigzag edge hosted FeN_4C_{10} structure at (a) T = 100 K, (b) T = 300 K and (c) T = 500 K. The EBET distribution for N atom in defected FeN_4C_{10} basal plane structure at (d) T = 100 K, (e) T = 300 K and (f) T = 500 K. The corresponding mean (μ) and standard deviation (σ) of temperature-dependent* EBET *distributions are shown in Figs 7(a) and 7(b) respectively.*

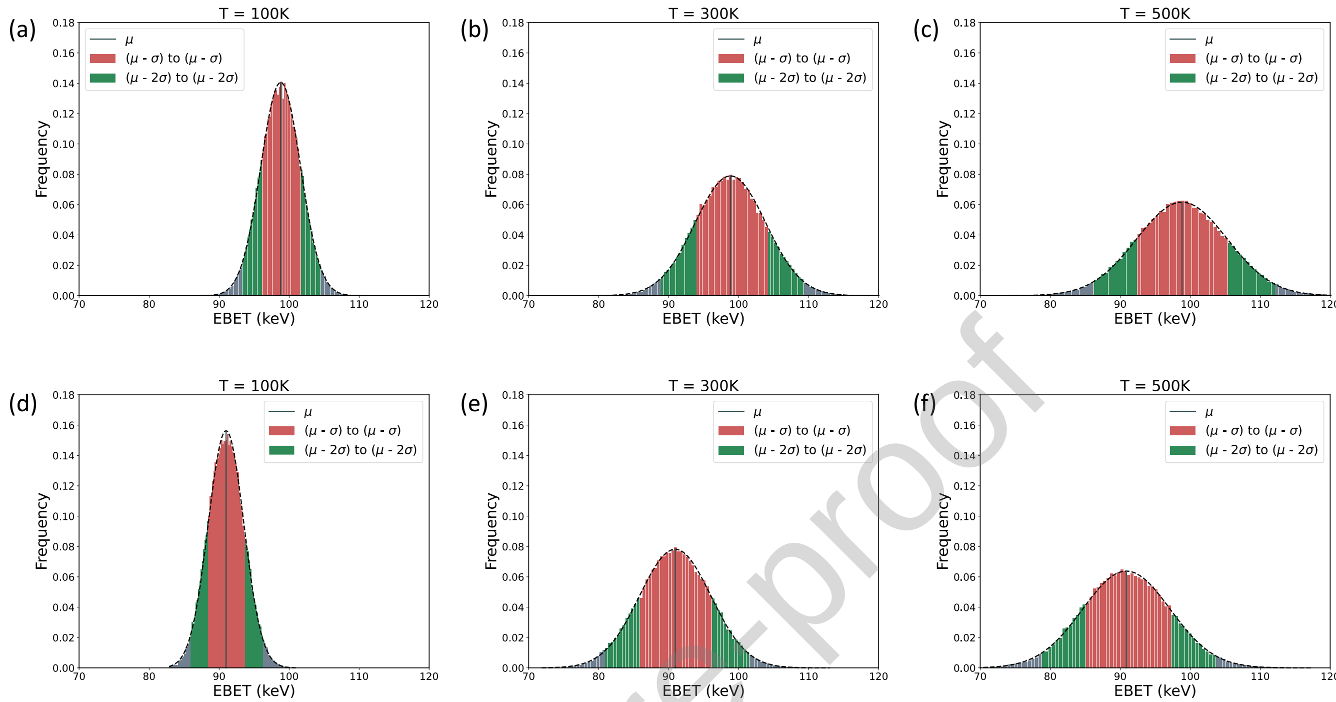

Figure S5: *The EBET distribution for N atom in FeN_4C_{12} basal plane structure at (a) T = 100 K, (b) T = 300 K and (c) T = 500 K. The EBET distribution for undercoordinated C atom in FeN_4C_{12} basal plane structure at (d) T = 100 K, (e) T = 300 K and (f) T = 500 K. The corresponding mean (μ) and standard deviation (σ) of temperature-dependent* EBET *distributions are shown in Figs 7(c) and 7(d) respectively.*

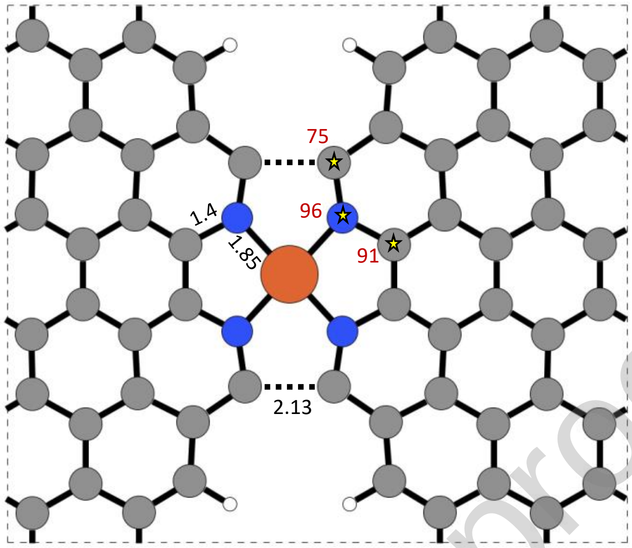

Figure S6: *Calculated 0 K EBET values for C and N atoms in FeN_4C_8 basal plane active site structure. Unit of EBET, reported in red, is in keV. C-C and C-N bond lengths, reported in black, are in Å. C, N and Fe atoms are shown in grey, blue and orange colors respectively.*

Table S1: The temperature-dependent mean (μ) and standard deviation (σ) of EBET distributions of various structures considered in this study.

Structure	Atom	0 K		100 K		300 K		500 K	
		μ	σ	μ	σ	μ	σ	μ	σ
FeN_4C_{10} - Basal Plane	N	88	0	87.69	2.88	87.70	4.76	87.68	6.22
FeN_4C_{10} - Edge	N	70	0	69.64	2.80	69.62	4.11	69.58	5.56
FeN_4C_{10} - C Vacancy	N	72	0	71.14	2.35	71.19	4.40	71.16	5.30
FeN_4C_{12}	N	99	0	98.79	2.84	98.83	5.05	98.82	6.47
N doped Graphene	N	99	0	98.59	2.90	98.59	5.47	98.58	6.49
Pristine Graphene	C	113	0	112.24	2.86	112.25	5.09	112.23	6.53
FeN_4C_{12}	C	91	0	90.99	2.55	90.94	5.10	90.88	6.25

Table S2: Comparison of *calculated 0 K EBET and KODTE values for C and N atoms in graphene and FeN_4C_x structures considered in this study.*

Structure	Atom	EBET (keV)	KODTE (eV)	Figure
Pristine graphene	C	113	22.92	2(a)
Bulk graphene with a mono vacancy	C	73	14.28	2(b)
	C	79	15.54	
N atom-doped in bulk graphene	N	99	17.01	2(c)
N atom doped in bulk graphene with an adjacent monovacancy	N	86	14.6	2(d)
Graphene nanoribbon zigzag edge	C	84	16.6	3(a)
Graphene nanoribbon armchair edge	C	94	18.75	3(b)
N atom at graphene nanoribbon zigzag edge	N	86	14.6	3(c)
N atom at graphene nanoribbon armchair edge	N	86	14.6	3(d)
FeN_4C_{10} basal plane	N	88	14.97	4(a)
	C	98	19.62	
	C	103	20.71	
FeN_4C_{10} at the zig-zag edge	N	70	11.71	4(b)
	C	104	20.93	
	C	89	17.67	
FeN_4C_{12} basal plane	N	99	17.01	4(c)
	C	98	19.62	
	C	103	20.71	
	C	91	18.1	
FeN_4C_{10} basal plane structure with C vacancy defects on the zig-zag site	N	76	12.79	4(d)
FeN_4C_{10} basal plane structure with C vacancy defects on the armchair site	N	72	12.07	4(e)
FeN_4C_8 basal plane	N	96	16.45	S6
	C	91	18.1	
	C	75	14.7	